

The Rising Sun Envelope Method: an automatic and accurate peak location technique for XANES measurements

Rafael Monteiro*

MathAM-OIL, AIST, c/o Advanced Institute for Materials Research, Tohoku University, Sendai, Japan

Itsuki Miyazato and Keisuke Takahashi†

Department of Chemistry, Hokkaido University, N-10 W-8, Sapporo 060-0810, Japan and

Center for Materials research by Information Integration (CMI²),

National Institute for Materials Science (NIMS), 1-2-1 Sengen, Tsukuba, Ibaraki 305-0047, Japan

(Dated: September 16, 2019)

The lack of theoretical understanding of X-Ray Absorption Near Edge Structure (XANES) spectroscopy makes the development of analysis tools for its study a necessity. Here, an algorithm for judicious choice of local minima and maxima points of XANES spectrum (experimental or simulated) is proposed, without any loss of information on peaks location nor on peak strength. We call it the *Rising Sun Envelope Method*, since it is based on successive regularizations of the spectral measurement that, according to parameter choices that are intrinsic to the measurements, keep peaks location and strength as invariants. This is the first method that finds peaks in XANES automatically, without depending on first derivative information. Nevertheless, a direct computation of Absorption-Edge is provided, where we avoid the issue inflection point computations based on the XANES second derivative, dealing instead with simpler computations of inflection points of higher quality cubic spline approximation. Besides applications of the algorithm to XANES, we illustrate further applications in Electron Energy Loss Spectroscopy (EELS) and Raman spectra.

INTRODUCTION

Atomic-Absorption Spectroscopy is a fundamental tool in Material Sciences for characterization of physical and chemical properties of materials [1]. In its foundations, the method is based on the photoelectric effect: upon interaction with photons or other particles the material's atoms absorb, emit, and reflect incoming radiation to neighboring atoms, thus providing information about the material's atomic structure and its complexities [2, §1-2]. In spite of its wide use, it is still a challenging task to extract meaningful and relevant information from spectra obtained in experimental measurements, and many theoretical questions in the field remain open.

One type of these measurements is known as X-Ray Absorption Near Edge Structure (XANES) [3–5] observed in X-ray Absorption Fine Structure (XAFS), where local structure and valence (or oxidation) state can be inferred from the way peaks amplify and shift horizontally when compared to peaks of a reference, non-oxidized, sample [6–10]. Several approaches to valence determination and material oxidation exist: for instance, Principal Components Analysis (PCA) is used to obtain *valence state fingerprinting*, i.e., characterization of valence state by interpolating it with a mixture of pure-valence species [11], a technique that is mathematically robust and powerful but rely on first derivative computations [12], which lacks on mathematical rigor, for the spectra

contains (non-differentiable) noise [13]. Direct use of first derivatives is also common [14, 15]. From a somewhat different perspective, Machine Learning (ML) techniques have been shown to be an effective method to unveil 3D structures in Nanoparticles [16], and characterize oxidation state by use of statistical methods [17]; in the context of XANES, it has been applied with the aim of predicting oxidation state by learning the peak shift [18]. Nevertheless, all these techniques rely on peak location, derivative computations, or peak shift estimates, but up to now no method can locate a sequence of peaks in an accurate fashion. It is worth to point out that regularization through smoothing is successfully used in linear filtering and denoising of images, because it averages noise and keep low frequencies [19]; however, it smears peak location and their strength, which are the objects we are mostly interested at [20, §6].

In this paper we take a step to address, and mitigate, the aforementioned issues of characterization of peak location in XANES by means that are not rigorous (as differentiation methods) proposing a new method that does not smear out neither peak location nor peak strength. As it is the case with several tools of signal processing, the Rising Sun Envelope Method relies on resolution parameters that set up thresholds for peak location based on both their height and how far apart they are. One of the building blocks of the paper is called the *Rising Sun Envelope Method* [21], in which an operator regularizes the XANES spectrum. The latter operator is applied successively in different energy range intervals, a process along which an invariant is kept at each step: in the corresponding interval, both the measurement and its regularization have their first peak located at the same

* monteirosilva-rafael@aist.go.jp

† miyazato@eng.hokudai.ac.jp, keisuke.takahashi@eng.hokudai.ac.jp

point. In each step these intervals get smaller, yielding a chained sequence of intervals and an increasing sequence of peak locations in the energy range.

Towards the end of the paper several applications are given: approximated splines are constructed, and an automatic and a more accurate way to locate inflection points is proposed. We remark that the latter do not rely on finite difference methods applied to the XANES measurement in order to find the second order derivatives, a computation that gives highly oscillatory results due to noise but, in spite of its poor quality, has been commonly used in the literature. Furthermore, the method provides a dimension reduction of the XANES measurement by judicious choice of interpolation points that can be then used for interpolation by polygonal, cubic splines, or clamped cubic splines glued up to first derivative. In the latter case, we assert the quality of our approximation by comparing the inflection points obtained with the second order derivative obtained by Athena, a well established software for XANES computations [22]. Finally, due to its generality, the Rising Sun envelope method can also be applied to other types of spectra, a fact that we illustrate with an application to Electron Energy Loss Spectroscopy (EELS) and Raman spectra.

THE RISING SUN AND VALLEY OF SHADOWS ASSOCIATED FUNCTIONS: AN ALGORITHM FOR PEAK LOCATION

Noise plagues spectral measurements with local maxima and minima, making the very distinction between peaks and pure noise fluctuations in many ways relying on the experimentalist's subjective judgment. The definitions in this section introduce two parameters that aim to both quantify and clarify the peak characterization.

In what follows, we shall consider a spectral measurement $\mu(E)$, where $e_{-\infty} \leq E \leq e_{+\infty}$ denotes the energy range of measurement on a meshgrid δn , where n is an integer and $\delta > 0$ the meshgrid width. The continuous function $\mu(E)$ represents the material's absorption at energy level E . We shall denote the restriction of this mapping to a smaller energy range $a \leq E \leq b$ by $\mu|_{[a,b]}(E)$. Without any loss of generality, we can normalize the spectrum and consider $\max_{e_{-\infty} \leq E \leq e_{+\infty}} \mu(E) - \min_{e_{-\infty} \leq E \leq e_{+\infty}} \mu(E) = 1$ and $\mu(e_{-\infty}) = 0$.

Definition I.1 (Peak criterion with thresholds (h_*, d_*))
Given the a measurement $\mu(E)$ in energy range $e_{-\infty} \leq E \leq e_{+\infty}$ and fixed constants $h_* > 0$ and $d_* > 0$. Let $e_{-\infty} \leq e_* < \bar{E} \leq e_{+\infty}$. We say that \bar{E} is a local maximum relative to e_* with thresholds (h_*, d_*) whenever

$$\left| \mu(\bar{E}) - \mu(e_*) \right| > h_*, \quad \text{and} \quad \mu(\bar{E}) \geq \mu(E) \quad (1)$$

holds for all $e_{-\infty} \leq E \leq e_{+\infty}$ with $|E - \bar{E}| \leq d_*$ (see Figure 1). Similarly, one says that point $e_* < \bar{E} \leq e_{+\infty}$ is a local

minimum relative to e_* with thresholds (h_*, d_*) whenever

$$\left| \mu(e_*) - \mu(\bar{E}) \right| > h_*, \quad \text{and} \quad \mu(\bar{E}) \leq \mu(E) \quad (2)$$

holds for all $e_{-\infty} \leq E \leq e_{+\infty}$ with $|E - \bar{E}| \leq d_*$.

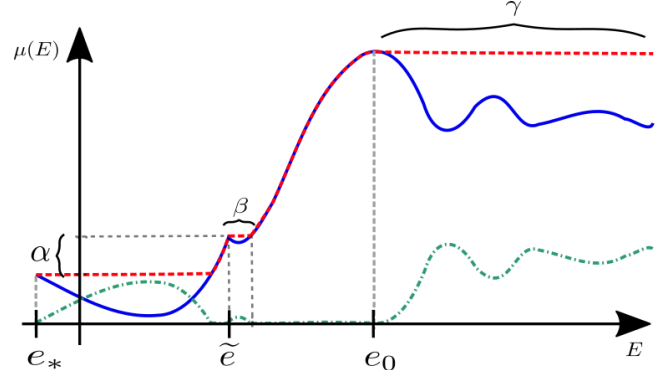


FIG. 1: An illustration of the use of (h_*, d_*) in peak finding: $\mu(E)$ is represented as full line (blue). When looking for a local maximum with threshold (h_*, d_*) relative to $(e_*, \mu(e_*))$, the first value in \tilde{e} is not considered a local maximum when $\alpha \leq h_*$; on the other hand, if $\alpha > h_*$, \tilde{e} is considered a local maximum only if $d_* < \beta$. The same analysis holds for \bar{E} , its relative height $\mu(\bar{E}) - \mu(e_*)$ and plateau size γ . The curve in red represents the Rising Sun function $\mathcal{R}_\mu(E)$ introduced in (4), a valuable tool to verify the conditions in Def. I.1.

The thresholds $h_* > 0$, $d_* > 0$ are quantities used to discern local maxima/minima as *pure noise* or true peaks. For instance, taking the limit $h_* \rightarrow +\infty$ (resp., taking the limit $d_* \rightarrow +\infty$), no local maxima/minima are found whereas, due to noise, in the limit $h_* \rightarrow 0$ (resp., $d_* \rightarrow \delta$) too many points are characterized as so. Thus, both thresholds must be tuned in order to capture intrinsic properties of the spectrum, like noise and relative distance between peaks; in that sense, both parameters play the role of *resolutions*, as in some tools of signal processing [23]. Furthermore, peak jumps display decaying properties, therefore it is important to take into account the relative dependence between successive maxima/minima, which is done by making each point a local maxima or minima with respect to the previous breakpoint. This remark leads to the following:

Definition I.2 (M-breakpoints with $(h_*^{(n)}, d_*^{(n)})$ threshold)
Consider a measurement $\mu(E)$ in the energy range $e_{-\infty} \leq E \leq e_{+\infty}$. Let $M > 0$ be a fixed integer, and $h_*^{(n)} > 0$, $d_*^{(n)} > 0$, where $0 \leq n \leq M$. Consider the points

$$e_{-\infty} < e_0 < e_1 < \dots < e_M \leq e_{+\infty}. \quad (3)$$

We say that this is a sequence (3) of M -breakpoints with $(h_*^{(n)}, d_*^{(n)})$ threshold whenever for all $n \geq 1$, each e_n with

n odd (resp., even) e_n is a local maximum (resp., local minimum) relative to e_{n-1} with threshold $(h_*, d_*^{(n)})$ of the truncated spectrum $\mu|_{[e_{n-1}, e_{+\infty}]}(E)$, that is, in the range $e_{n-1} \leq E \leq e_{+\infty}$.

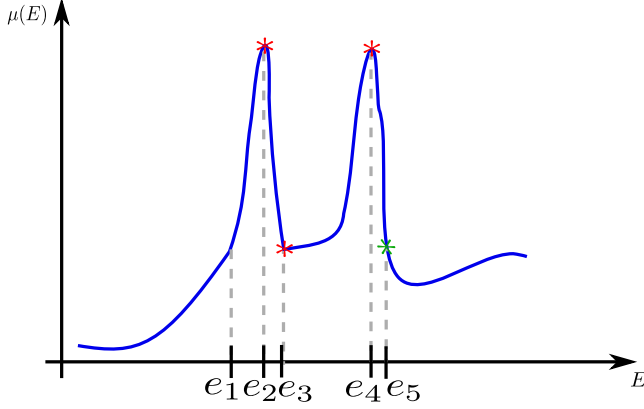


FIG. 2: Sketch of XANES spectrum and breakpoints e_1 , e_3 and e_4 . Considering $e_3 - e_0 < d_* < e_4 - e_1$, we have that e_1 and e_3 are local maxima with in a neighborhood of size d_* , while e_3 is not a local minimum in a neighborhood of same size due to the point e_0 . Notice that the sharp decay of $\mu(E)$ in the range $e_1 \leq E \leq e_3$ is controlled by the threshold h_* . Finally, note that if $e_5 - e_1 < d_*$ then the algorithm skip all the points in the range $e_1 \leq E \leq e_4$ in the search for local minimum, being this one of the main reasons for readapting the threshold d_* as the peak search happens; see also Figure 3 for more details.

It is clear that a local maximum e_0 relative to $e_{-\infty}$ with threshold $(h_*, d_*^{(n)})$ consists of a 1-breakpoint with $(h_*, d_*^{(n)})$ threshold. The previous definition takes into account the order of the peaks and their sequential, pairwise, relative height. This step also implies that all the elements e_n in (3) with an even index n (resp., odd index n) are apart by a distance at least $d_*^{(n)}$.

Several aspects of the previous definitions are worth of discussion. For simplicity, consider the thresholds $(h_*^{(n)}, d_*^{(n)})$ constants in n , assuming the value (h_*, d_*) :

- (C1) There is a trade-off between h_* and d_* , and varying these quantities as the algorithm evolves is important to avoid local minima between two local maxima that would otherwise go undetected, as discussed in Figure 2. Three mechanisms are in place to avoid this problem: (a) sharp variations in spectrum behavior are captured by the oscillation threshold (that is, h_* large), (b) thresholds can vary throughout the search for breakpoints (see the algorithm 1 and Figure 5), and the most effective of them all (c), called the *hidden peak tricks*, two techniques that introduce a spatial delay in

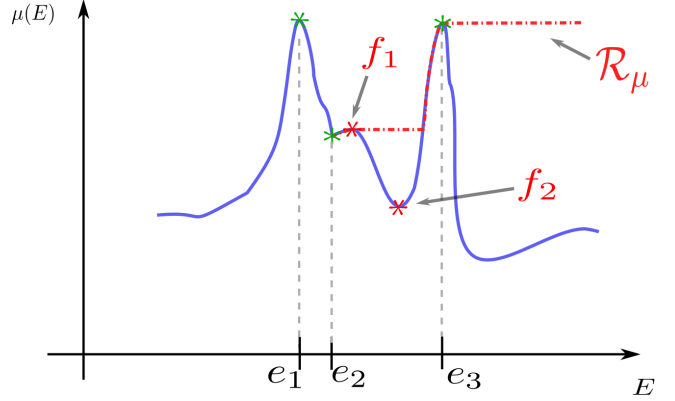


FIG. 3: Sketch of the *hidden peak trick* in a XANES spectrum $\mu(E)$. Considering an iteration from the local minimum e_2 with thresholds $(h^{(2)}, d^{(2)})$, after which the algorithm constructs a Rising sun function \mathcal{R}_μ . When $|\mu(f_1) - \mu(e_2)| < h^{(2)} < |\mu(e_3) - \mu(e_2)|$, the algorithm sets e_3 as the next breakpoint, i.e., as local maximum, while skipping all the points in the range $e_2 \leq E \leq e_3$. This is problematic, for it could clearly miss local minima as f_2 .

The algorithm was implemented to check this case, allowing for two options: (i) e_2 is set as f_2 , or (ii) e_3 is set as f_1 ; the algorithm runs from e_3 after this reassignment.

the algorithm in order to verify whether its breakpoints are indeed local minimum/maximum, in some cases at risk of violating the peak threshold (see Figure 3).

- (C2) For any $n > 1$, it is possible that the element e_n in a M-breakpoint sequence with threshold (h_*, d_*) is a local minimum/maximum of $\mu|_{[e_{n-1}, e_{+\infty}]}(E)$, but not of $\mu|_{[e_{-\infty}, e_{+\infty}]}(E)$ (see Figure 2). However, for peaks found without using the *hidden peak trick* it is true that the distance between any two of them that are successive local maxima or local minima is bigger than d_* ; hence, they are all peaks with threshold (h_*, d_*) in $[e_0, e_{+\infty}]$. Last, one can deduce from Def. I.1 that the distance between peaks gives an estimate of the plateau sizes of the associated Rising Sun functions used to locate them;
- (C3) The number M is an upper bound on the number of peaks to be sought. In fact, the algorithm can stop before that many points are found: this is verified by checking if end of the range of measurement has been reached. Indeed, checking the Definition I.1 close to the endpoint can be an issue which we overcome by embedding the spectra in a higher dimensional space in a trivial fashion, that is, gluing the rightmost point to a constant in a continuous fashion; the latter does not affect peak

location, peak height, nor the oscillation function (see Definition I.4).

The following auxiliary constructions are useful to verify the properties in the previous definitions.

Definition I.3 (Rising Sun and Valley of Shadows)

Given the XANES measurement $\mu(E)$ in the energy range $e_{-\infty} \leq E \leq e_{+\infty}$, we define the Rising Sun operator

$$\mathcal{R}_\mu(E) = \max_{e_{-\infty} \leq x \leq E} \mu(x), \quad (4)$$

where we call the function $\mathcal{R}_\mu(E)$ the Rising Sun function (associated to $\mu(E)$). We also define the Valley of Shadows operator,

$$\mathcal{V}_\mu(E) = \mathcal{R}_\mu(E) - \mu(E), \quad (5)$$

where we call the mapping $\mathcal{V}_\mu(E)$ the Valley of Shadows function (associated to $\mu(E)$).

The following properties are an immediate consequence of the definition I.1 and the construction of the Rising Sun and Valley of Shadow functions $\mathcal{R}_\mu(E), \mathcal{V}_\mu(E)$, respectively.

- (R1) The function $\mathcal{R}_\mu(E)$ is non-decreasing. Furthermore, the inequality $\mu(E) \leq \mathcal{R}_\mu(E)$ (equivalently, $0 \leq \mathcal{V}_\mu(E)$) holds;
- (R2) Any non-decreasing function is invariant under the Rising Sun operator. In particular, the Rising Sun function is a fixed point of the Rising Sun operator, namely, $\mathcal{R}_{\mathcal{R}_\mu}(E) = \mathcal{R}_\mu(E)$;
- (R3) Let the point \bar{e}_1 be the first local maximum of μ in the range $e_{-\infty} \leq E \leq e_{+\infty}$ with threshold (h_*, d_*) . Then, \bar{e}_1 is the local maximum of \mathcal{R}_μ in the range $e_{-\infty} \leq E \leq e_{+\infty}$ with threshold (h_*, d_*) , that is,

$$\mu(\bar{e}_1) = \mathcal{R}_\mu(\bar{e}_1) = \mathcal{R}_\mu(E), \quad \bar{e}_1 \leq E < \bar{e}_1 + d_*.$$

In other words, the functions $\mu(E)$ and its associated Rising Sun function \mathcal{R}_μ have the same first maximum in the range $e_{-\infty} \leq E \leq e_{+\infty}$;

- (R4) Consider the first peak \bar{e}_1 with threshold (h_*, d_*) . Let \bar{e}_2 be the first local maximum with threshold (h_*, d_*) of $\mathcal{V}_\mu(E)$ in the range $\bar{e}_1 \leq E \leq e_{+\infty}$. Then $(\bar{e}_2, \mu(\bar{e}_2))$ is a local minimum of $\mu|_{[e_0, e_{+\infty}]}(E)$ with threshold (h_*, d_*) . Furthermore, $e_{-\infty} \leq e_0 < e_1 \leq e_{+\infty}$ is a sequence of 2-breakpoints with threshold (h_*, d_*) .

We carefully explain each of these properties, as they are used in the implementation of Algorithm 1: properties in (R1) show that the Rising Sun function $\mathcal{R}_\mu(E)$ is the smallest non-decreasing majorant of $\mu(E)$; (R2) shows

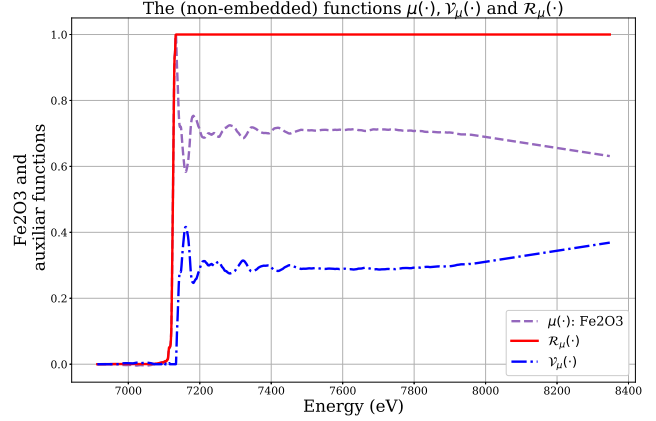


FIG. 4: A spectral measurement $\mu(E)$ of Fe_2O_3 , its associated Rising Sun $\mathcal{R}_\mu(E)$ and Valley of Shadows functions $\mathcal{V}_\mu(E)$. Notice the correspondence between local minima of $\mu(E)$ with local maxima of $\mathcal{V}_\mu(E)$.

that the family of non-decreasing functions is closed under the action of the Rising Sun operator; (R3) asserts the invariance of the location and strength of the first local maximum with threshold (h_*, d_*) ; (R4) provides the main idea of the algorithms, giving the foundation for the recursion in the sequence of smaller intervals $[e_{n-1}, e_{+\infty}] \supset [e_n, e_{+\infty}]$.

Quantification of thresholds (h_, d_*) .* In the algorithm, the thresholds $(h_*^{(0)}, d_*^{(0)})$ are initialized before the peak search begins. Both quantities are highly dependent on the nature of the spectroscopy problem one deals with (see also Section): easier to quantify, h_* denotes a the threshold for peak height aiming to distinguish peaks from random noise fluctuations; it is mostly dependent on the statistical error quantification or, more precisely, on the effect of noise on the regularity of $\mu(E)$. We estimate it using an oscillation function:

Definition I.4 (Oscillation function) We define the oscillation threshold h_*^μ of $\mu(E)$ as

$$h_* = \omega_*^\mu(\delta), \quad \text{for } \omega_*^\mu(j\delta) = \max_{|E-E'| \leq j\delta} |\mu(E) - \mu(E')|.$$

where $\omega_*^\mu(E)$ is called oscillation function of $\mu(E)$.

It is straightforward to show that $\omega_*^{\mathcal{R}_\mu}(j\delta) \leq \omega_*^\mu(j\delta)$, which amounts to saying that $\mathcal{R}_\mu(E)$ is more regular (less noisy) than the function $\mu(E)$ it is associated to; this can be seen as a *denoising* effect, even though the analysis is not carried out in frequency space.

In contrast to the previous case, the parameter d_* is heavily dependent on the distribution of peaks throughout the spectrum, which a priori is unknown. By the construction of the Rising Sun function allied to (C2) we conclude that information about the distance between successive peaks provide estimates about the minimum size

of the associated Rising Sun's plateaus. Thus, to initialize the code an estimate of this distance is given by $d_*^{(0)}$, which we take to be

$$d_*^{(0)} = x_1 - x_0, \quad (6)$$

where we first compute x_1 as local maximum with threshold $(\lambda_1 h_*, \lambda_2 d_*)$ relative to $(e_{-\infty}, \mu(e_{-\infty}))$; the quantities λ_1, λ_2 are positive hyperparameters, which in computations for XANES were set as $\lambda_1 = 4$ and $\lambda_2 = \frac{1}{4}$. It is clear from it's construction that we have $e_0 = x_1$. Subsequently, we define x_0 as

$$x_0 = \max \left\{ e_{-\infty} \leq E \leq e_1 \mid \mu(E) \leq \mu(-\infty) + h_*^{(0)} \right\}. \quad (7)$$

We can define what we call the *min max* method:

$$\begin{aligned} \alpha_{\min \max}^{(n)} &= \frac{\max_{\tilde{x}, \tilde{y} \in [e_n, e_{+\infty}]} |\mu(\tilde{x}) - \mu(\tilde{y})|}{\max_{x, y \in [e_{-\infty}, e_{+\infty}]} |\mu(x) - \mu(y)|}, \\ h_*^{(n+1)} &= \alpha_{\min \max}^{(n)} \cdot h_*^{(n)}, \\ d_*^{(n+1)} &= \alpha_{\min \max}^{(n)} \cdot \max \left\{ \text{average} \left(d_*^{(k)} \right)_{0 \leq k \leq n}, 2 \right\}. \end{aligned} \quad (8)$$

Clearly, variations of the above give different results, specially for peaks that are harder to distinguish from pure noise spikes. An immediate objection to (8) is the use of peaks height's decay information to infer the peak distance information, which give good results for small number of peaks, but is nonetheless far-fetched. For that reason other methods were also designed; for instance, the threshold formula is

$$d_*^{(n)} = \max \left\{ \left(\lambda_3 e^{-n} + \frac{n}{2} \right) \frac{2L}{n+1}, 2 \right\}, \quad (9)$$

where λ_3 is a hyperparameter. Each method estimates the quantity L in a different way:

- i. (*Regression*) Given the location of i peaks, estimate the plateau size of the next one by doing the a regression of type

$$L = \alpha_d \exp \{ \beta_d (i+1) \}, \quad (10)$$

where α_d and β_d are estimated using the points $(j, d_*^{(j)})$ for $0 \leq j \leq i$.

- ii. (*Learn to trust*) Given the location of i peaks, estimate the the quantity L as

$$L = \text{average} \left(d_*^{(k)} \right)_{0 \leq k \leq n}. \quad (11)$$

Assuming L fixed, note that when $n = 0$ the estimate (9) gives

$$d_*^{(0)} = \max \{ \lambda_3 L, 2 \};$$

on the other hand, as $n \rightarrow +\infty$

$$\lim_{n \rightarrow +\infty} d_*^{(n)} = \max \{ L, 2 \}.$$

In this case, the initial guess given by the hyperparameter λ_3 plays an important role in the search of peaks immediately after the first located peak; however, this guess lose importance as the method gather more data from previous peaks, eventually *learning from it*. In Fig. 5 we plot a comparison between several methods to estimate the distance; see [24] for further details.

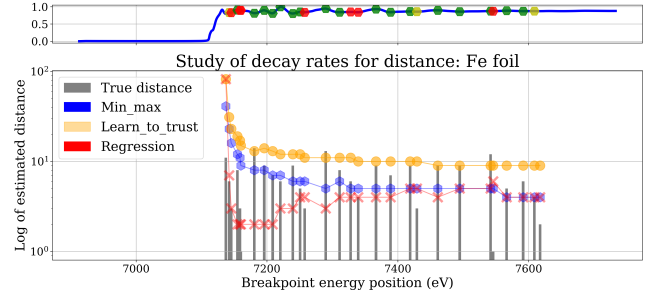


FIG. 5: Some statistics for the threshold of distance *Fe foil*, which is then used as an estimate for the size of plateaus and, conveniently, as thresholds $d_*^{(n)}$. In all of which the estimate for $d_*^{(0)}$ is given by (6).

A few more words about the *regression method* are necessary: in the way it has been applied to estimate $d_*^{(n+1)}$ from $(h_*^{(j)}, d_*^{(j)})_{1 \leq j \leq n}$ it can also be applied to estimate $h_*^{(n+1)}$. Indeed, at the n th peak we would like to find a good candidate for the threshold $h_*^{(n+1)}$; recall that the location of the $(n+1)$ -th peak is unknown. We proceed as follows: a linear regression of $\mu|_{[e_n, e_n + 2d_*^{(n+1)}}$ on $E|_{[e_n, e_n + 2d_*^{(n+1)}}$, where $d_*^{(n+1)}$ is computed using (9) with L as in (10). We estimate and write the error in the regression as $\hat{\sigma}(E)$ (see [20, §8, Eq. (8.4)]), from which we obtain two curves,

$$\widehat{\mu^{(\pm)}}(E) = \underbrace{\beta_0 + \beta_1 E}_{\text{linear prediction}} \pm \lambda_4 \cdot \hat{\sigma}(E), \quad (12)$$

for $e_n \leq E \leq e_n + 2d_*^{(n+1)}$ and λ_4 a hyperparameter (in our case set as $\lambda_4 = 3$ throughout computations). Now, define $S_{\text{regression}} \equiv \max_{\tilde{x}, \tilde{y} \in [e_n, e_n + 2d_*^{(n+1)]]} |\widehat{\mu^{(+)}}(\tilde{x}) - \widehat{\mu^{(-)}}(\tilde{y})|$, which gives an estimate on the jump in intensity between the n -th peak (already known) and the $(n+1)$ -th peak (unknown). We have then the *regression method*, a slight variation of (8),

$$\begin{aligned} \alpha_{\text{regression}}^{(n)} &= \frac{S_{\text{regression}}}{\text{average of previous jumps}}, \\ h_*^{(n+1)} &= \alpha_{\text{regression}}^{(n)} \cdot h_*^{(n)}. \end{aligned} \quad (13)$$

The method is illustrated in Fig. 6.

Searching on the other side of the Near-Edge peak: the reflection method. By construction, the algorithm starts

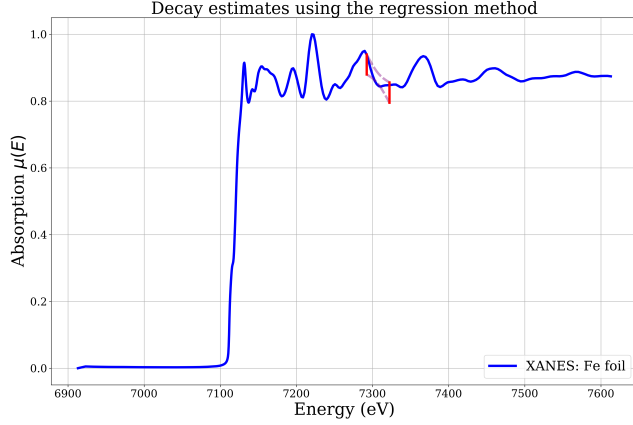


FIG. 6: An illustration of the *regression method* applied to Fe foil. The error curves (12) are in purple, while the red curves give the error range at the beginning and at the end of the regression range.

at e_0 , somehow ignoring any peak to the left of it. This is somewhat intentional, and is done for two reasons: first, away from the peak-edge (the “0th peak”), peaks on both sides decay at different rates; second, the algorithm can use itself in a recursive fashion to search for peaks on the left side once it has finished the search on the right side. The latter is carried out by reflection of the spectrum about the peak e_0 , $\tilde{\mu}(E) \equiv \mu(e_0 + e_{-\infty} - E)$ and restricting the range of search to $e_{-\infty} \leq E \leq e_{-\infty} + e_0$; the initial thresholds $\tilde{h}_*^{(0)}$ and $\tilde{d}_*^{(0)}$ are estimated from $h_*^{(n)}$ and $d_*^{(n)}$. The output is shown in Figure 7.

Pathological measurements, threshold readjustment, and the role of noise. We remark that the algorithm takes advantage of the presence of noise: in the case of an unsuccessful search for peaks with thresholds (h_*, d_*) , the algorithm readjust the quantities to

$$h_* \leftarrow \lambda_5 h_*, \quad \text{and} \quad d_* \leftarrow d_* - 1,$$

either in an alternate fashion or simultaneously (also a hyperparameter, we set $\lambda_5 = 0.9$ throughout our computations); see [24] for further details. In contrast, the algorithm would stop in the first peak of a polygonal curve that has plateaus bigger than d_* ; the implementation takes these as pathological cases, for they are not expected in XANES. Moreover,

FURTHER APPLICATIONS

A dimension reduction method using judiciously chosen breakpoints for interpolation. With the breakpoints $e_{-\infty} \leq e_{-M_{-\infty}} \leq \dots \leq e_0 \leq e_1 \leq \dots \leq e_{M_{\infty}} \leq e_{+\infty}$ in hands we now look for a lower dimensional representation of $\mu(E)$ in the energy range $e_{-\infty} \leq E \leq e_{+\infty}$. That is, given

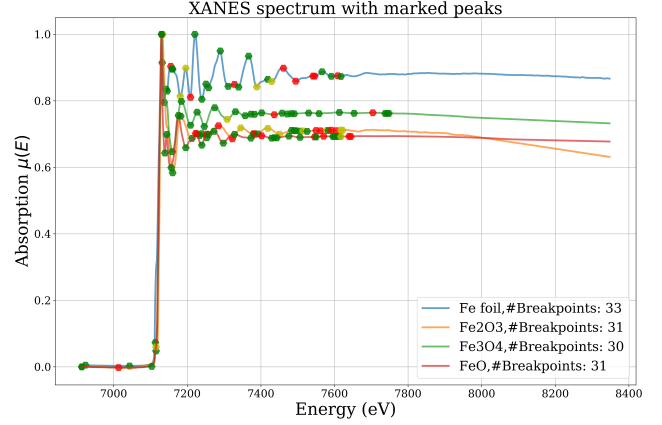


FIG. 7: An example of peak localization in Fe samples. For peaks on the right (resp. left) of the 0th peak, i.e., peak e_n with $n > 0$ (resp. $n < 0$), the color of the marker indicates the ratio between oscillation in $\mu|_{[e_n, e_{+\infty}]}$ (resp. $\mu|_{[e_{-\infty}, e_n]}$) and the amount of jump to the previous peak; similarly, the color on the 0th peak denotes the ratio between oscillation in the whole energy range $[e_{-\infty}, e_{+\infty}]$ and its jump (or estimated jump) to previous peak: the color is green whenever this ratio is less than 1, yellow for ratio in between 1 and 2, and red whenever the ratio is above 3. This ratio can be used as a measure of “peak relevance”, allowing one to introduce scores to classify the quality of the found peaks.

the points $(e_m, \mu(e_m))_{-M_{-\infty} \leq m \leq M_{\infty}}$ we can choose several methods to interpolate the given spectrum $\mu(E)$ (see Figure 8). The number of points in the interpolation can be increased by further refinement of the intervals $[e_m, e_{m+1}]$, for $m \in \{-M_{-\infty}, \dots, M_{\infty} - 1\}$. The breakpoints

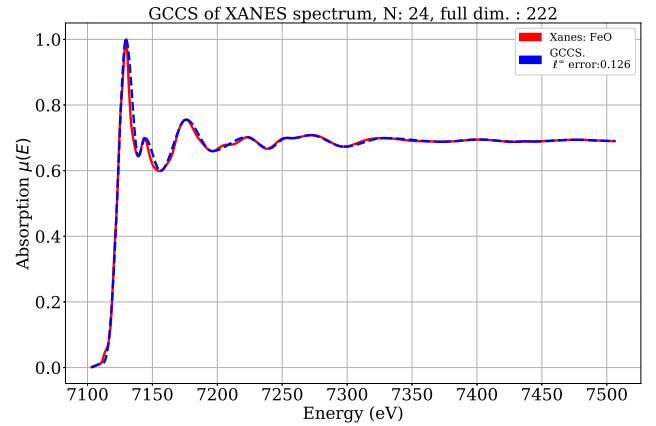


FIG. 8: Glued Clamped Cubic Spline for FeO , with 24 interpolation points, using judiciously chosen interpolating points chosen by the Rising Sun Envelope Method.

e_m , for $-M_\infty \leq m \leq M_\infty$ provide a partition of the energy range $e_{-\infty} \leq E \leq e_{+\infty}$ into intervals of *almost monotonic behavior*. In passing, it allows for the use of interpolation methods that exploit this fact. Indeed, in between two successive breakpoints we interpolated a cubic clamped spline, that is, a spline in with zero derivative at its endpoints; we call it Glued Clamped Cubic Spline (GCCS) the resulting concatenation of the these clamped cubic splines along the interpolated intervals, a result that provides a better quality of approximation when compared to other types of interpolations (see Figure 9). Other techniques have also been implemented; for instance: padding the endpoints of the XANES spectrum with constants was used to tame the wild behavior of interpolation near the boundaries [20, §5.2.1], where the spectrum was padded, interpolated and then truncated to the relevant energy region.

In Figures 9 (resp., 10) we show the ℓ^∞ interpolation error, i.e., maximum of absolute difference, (resp., ℓ^1 interpolation error, i.e., sum of the absolute differences). We compare our result to other Cubic Spline interpolations with equally spaced meshgrids with same number or points. The error using Glued Clamped Cubic Splines (GCCS) is mostly smaller in lower dimensions, while it gets similar as the dimension (number of interpolation points) increases.

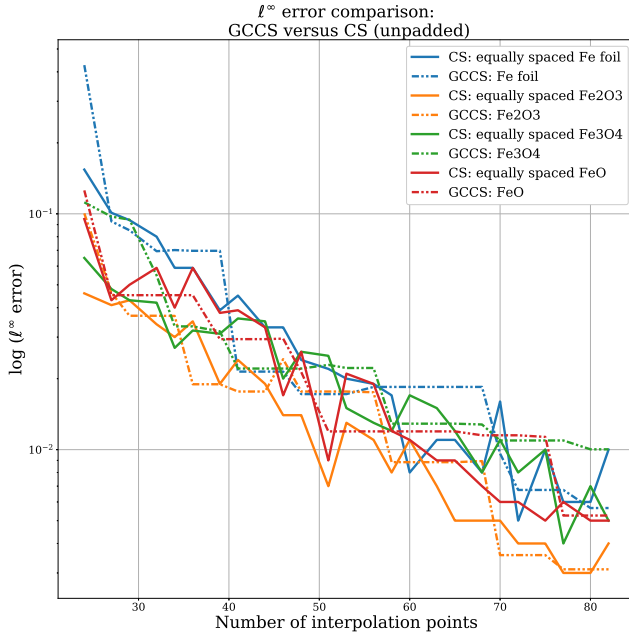


FIG. 9: The judicious choice of interpolation points provided by our algorithm leads to better approximation result in ℓ^∞ norm, and also to exact location of peaks. Comparison between Glued Clamped Cubic Spline (GCCS) method and Cubic Splines (CS).

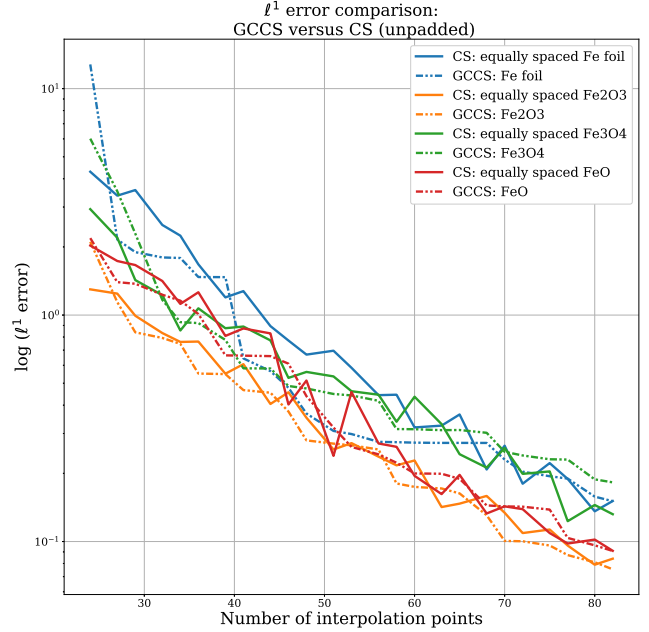


FIG. 10: Study of approximation error of interpolation in ℓ^1 norm comparing the Glued Clamped Cubic Splines (GCCS) method to Cubic Splines (CS) interpolation using equally spaced meshgrid.

Inflection point calculation. In figure 11 the first derivative of the interpolant approximation. For peak location purposes, plotting the first derivative is unnecessary because the Rising Sun Envelope Method, for given thresholds, finds exact peak location. Nevertheless, it is common in the literature to associate the highest value of the first derivative to the point of highest absorption, which is also called the *Absorption Edge*. As an inflection point of the XANES measurement, the second derivative of the measurement is commonly computed in spite of its poor quality due to noise (see Figure 11). For comparison, we plot the first derivative of our interpolant and all its inflection points, which are robust and more amenable to computation due to the good differentiability properties of the clamped splines in each interval they are defined in. The poor information given by the second derivative of the spectrum prevents much information to be obtained from it whereas, in contrast, the quality of the inflection points found using the clamped splines approximation. We highlight that the approximation used in Figure 11 requires only 28 interpolation points out of 418, that is, only approximately 6% of the whole spectrum information was used.

Applications to EELS and Raman spectra. The characterization of peaks shift and its intensity in Electron Energy Loss Spectroscopy (EELS) have a similar reason as that in XANES, therefore it is a natural object for validation of our code (see Figure 12). In Fig. 13 the Ris-

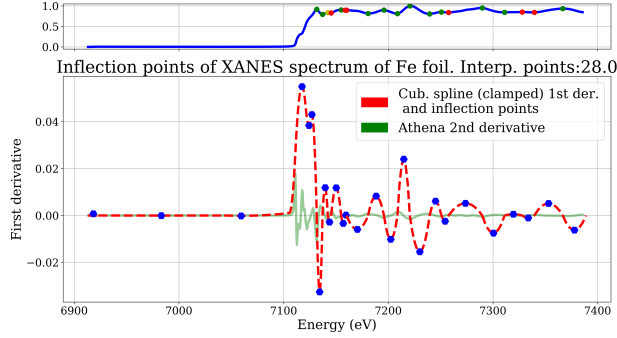


FIG. 11: Inflection points of XANES measurement, computed from approximation curved. In comparison, the second derivative of the XANES spectrum found using *Athena* [22] is also given, noticeably more susceptible to noise.

ing Sun Envelope Method is applied to Raman Spectra of Sulphur. In Raman Spectroscopy peak location is used as a initial that precedes Gaussian, or other type of, fitting [25]; in this case, knowledge of peak position and its intensity helps in qualitative and quantitative comparison between spectrum and data libraries, which is a fundamental step in Raman spectroscopy. It is worth to point out that in Raman the distribution of peaks is more erratic, and peak strengths do not visibly seem to decay around a particular peak. Nevertheless, the Rising Sun Envelope Method can still be applied in this case.

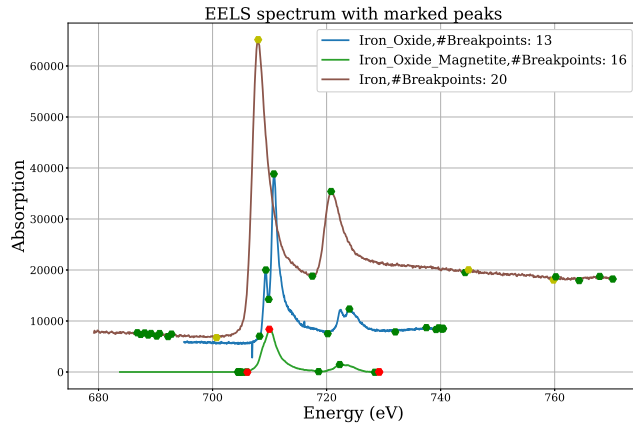


FIG. 12: EELS spectra of Iron, Iron oxide, and Iron oxide magnetite with marked peaks; data source [26].

DISCUSSION AND CONCLUSIONS

The Rising Sun Envelope Method is accurate in locating peak intensity and peak location, allowing for discernment between *true peaks* from *random noise spikes*. The method takes into account the intrinsic noise of the

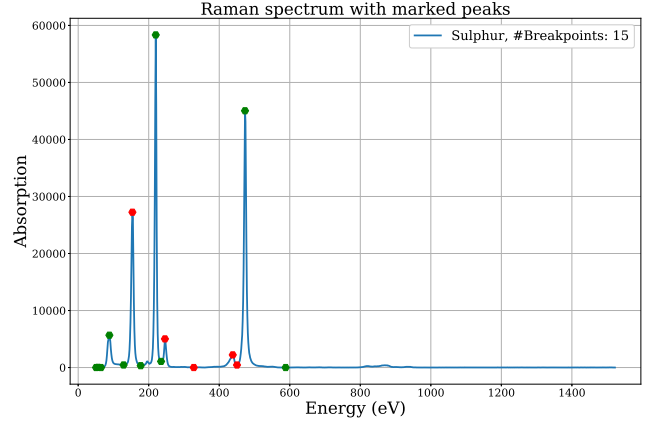


FIG. 13: Raman spectra of depolarized Sulphur with marked peaks; data source[27].

measurement, which makes it suitable for continuous, but noisy, functions, and in particular for experimental measurements. It provides an automated approach to peak decomposition that uses the pointwise structure of the function and its intrinsic properties.

Our results also provide a more accurate way to locate the peak-edge region (see Figure 11); overall, it is the first case in which this computation can be fully performed automatically.

The choice for peaks as interpolating points in polygonal or cubic spline approximations is shown to be an effective way to reduce the dimension of the spectral measurements. This choice is faithful to two qualities that are crucial in material oxidation analysis: peak location and its strength (see Figure 7). In effect, there are many reasons to pursue this kind of reductions: the first can be found in the initial steps of the ML model in [18], where a measure of the peak shift was the way the authors found to overcome this high dimensionality issue, considerably reducing the dimension of each XANES measurement in a way that is physically consistent with experiments; the Rising Sun Envelope method was originally developed with the intent of engineering more accurate horizontal peak shift features. Another reason to pursue dimensional reduction is due to the difference between the dimension of spectral measurements (of order $\mathcal{O}(1000)$) and the sample size (of order $\mathcal{O}(100)$), yielding disparity between number of variables and number of constraints that prevents good fitting and the use of non-local Machine Learning methods (as Convolution Neural Networks) [28, §9]. Still, a third reason can be presented: the availability of more data of XANES measurements by initiatives like [29] will make the use ML and other Artificial Intelligence methods more common, accurate, and effective in the field of Material Sciences [30, 31]; the clamped spline interpolations we found not only reduce the dimension of the data, but further capture the com-

plexity of the XANES measurement in a regularized fashion that is accurate and representative.

Numerical code for this paper has been written in Python and is available on [24].

ACKNOWLEDGMENT

This work is funded by Japan Science and Technology Agency(JST) CREST Grant Number JPMJCR17P2, JSPS KAKENHI Grant-in-Aid for Young Scientists (B) Grant Number JP17K14803, and Materials research by Information Integration (MI²I) Initiative project of the Support Program for Starting Up Innovation Hub from JST. XAFS spectrum data is utilized from XAFS database available in Institute of Catalysis, Hokkaido University [32], and XAFS Spectra Library in the Center for Advanced Radiation Sources(CARS), the University of Chicago [33]. R. M. is grateful to the MathAM-Oil group (AIST/AIMR, Tohoku Univ.) for several comments and suggestions offered during a seminar where this project was presented, specially to A. Watanabe's (AIST) helpful comments on Raman spectra.

Competing financial interests

The authors declare no competing financial interests.

-
- [1] D. C. Koningsberger and R. e. . Prins, *X-ray absorption: principles, applications, techniques of EXAFS, SEXAFS, and XANES*. United States: John Wiley and Sons, New York, NY, 1988.
 - [2] G. Bunker, *Introduction to XAFS: a practical guide to X-ray absorption fine structure spectroscopy*. Cambridge University Press, 2010.
 - [3] A. I. Frenkel, J. A. Rodriguez, and J. G. Chen, "Synchrotron techniques for in situ catalytic studies: capabilities, challenges, and opportunities," *Acs Catalysis*, vol. 2, no. 11, pp. 2269–2280, 2012.
 - [4] A. Kuzmin and J. Chaboy, "EXAFS and XANES analysis of oxides at the nanoscale," *IUCrJ*, vol. 1, no. 6, pp. 571–589, 2014.
 - [5] M. Neville, "Fundamentals of XAFS," *Reviews in Mineralogy and Geochemistry*, vol. 78, no. 1, pp. 33–74, 2014.
 - [6] J. Zhao, F. Huggins, Z. Feng, F. Lu, N. Shah, and G. Huffman, "Structure of a Nanophase Iron Oxide Catalyst," *Journal of Catalysis*, vol. 143, no. 2, pp. 499–509, 1993.
 - [7] M. Belli, A. Scafati, A. Bianconi, S. Mobilio, L. Palladino, A. Reale, and E. Burattini, "X-ray absorption near edge structures (XANES) in simple and complex Mn compounds," *Solid State Communications*, vol. 35, no. 4, pp. 355–361, 1980.
 - [8] N. M. Souza-Neto, J. Zhao, E. E. Alp, G. Shen, S. V. Sinoeikin, G. Lapertot, and D. Haskel, "Reentrant valence transition in euo at high pressures: Beyond the bond-valence model," *Phys. Rev. Lett.*, vol. 109, p. 026403, Jul 2012.
 - [9] L. Lin, S. Yao, R. Gao, X. Liang, Q. Yu, Y. Deng, J. Liu,

Algorithm 1: Rising sun Algorithm for peak decomposition.

Result: Rising Sun Envelope Method for peak location of a spectral measurement

```

/* Forward passage */
Data: Given a measurement  $\mu(E)$  in the range
 $e_{-\infty} \leq E \leq e_{+\infty}$ , threshold parameters  $(h_*^{(0)}, d_*^{(0)})$ ,
integers  $M_{\text{after}} > 0$  and  $M_{\text{before}} \geq 0$ , and two sets of
hyperparameters  $\mathcal{H}_{\text{after}}$  and  $\mathcal{H}_{\text{before}}$ 
while  $0 \leq n < M_{\text{after}}$  do
  if  $n$  is even then
    Set  $f(E) = \mu|_{[e_n, e_{+\infty}]}(E)$  and compute the Rising
    Sund function  $\mathcal{R}_f(E)$  on energy range
     $e_n \leq E \leq e_{+\infty}$ ;
    if the first local maximum  $\bar{E}$  of  $\mathcal{R}_f(E)$  with
    threshold  $(h_*^{(n)}, d_*^{(n)})$  exists then
      Set  $e_{n+1} \leftarrow \bar{E}$ ;
       $n \leftarrow n + 1$  and continue;
    else
      "only i-breakpoints could be found", hence
      break;
    end
  else
    With  $f(E)$  as before, compute the Valley of
    Shadows function  $\mathcal{V}_f(E) = \mathcal{R}_f(E) - f(E)$ ; set
     $f(E) = \mathcal{V}_f|_{[e_n, e_{+\infty}]}(E)$ ;
    if the first local maximum  $\underline{E}$  of  $f(E)$  with threshold
     $(h_*^{(n)}, d_*^{(n)})$  exists then
      Set  $e_{n+1} \leftarrow \underline{E}$ ;
       $n \leftarrow n + 1$  and continue;
    else
      "only i-breakpoints could be found", hence
      break;
    end
  end
end
/* Reverse parrage: search on the left side of the
0th peak */
if  $M_{\text{before}} > 0$  then
  Define  $\tilde{\mu}(E) = \mu(e_{-\infty} + e_0 - E)$  in the range
   $e_{-\infty} \leq E \leq e_0 + e_{-\infty}$ ;
  Run the previous code on threshold parameters
   $(h_*^{(0)}, d_*^{(0)})$ ,  $\widetilde{M}_{\text{after}} = M_{\text{before}}$ ,  $\widetilde{M}_{\text{before}} = 0$ ,
  and two sets of hyperparameters  $\widetilde{\mathcal{H}}_{\text{after}} \equiv \mathcal{H}_{\text{before}}$ 
  and  $\widetilde{\mathcal{H}}_{\text{before}} \equiv \emptyset$ ;
end

```

M. Peng, Z. Jiang, S. Li, *et al.*, "A highly CO-tolerant atomically dispersed Pt catalyst for chemoselective hydrogenation," *Nature nanotechnology*, vol. 14, no. 4, p. 354, 2019.

- [10] J. Mao, W. Chen, D. He, J. Wan, J. Pei, J. Dong, Y. Wang, P. An, Z. Jin, W. Xing, *et al.*, "Design of ultrathin Pt-Mo-Ni nanowire catalysts for ethanol electrooxidation," *Science advances*, vol. 3, no. 8, p. e1603068, 2017.
- [11] A. Manceau, M. A. Marcus, and S. Grangeon, "Determination of Mn valence states in mixed-valent manganates by XANES spectroscopy," *American Mineralogist*, vol. 97, pp. 816–827, 05 2012.

- [12] A. Manceau, M. Marcus, and T. Lenoir, "Estimating the number of pure chemical components in a mixture by X-ray absorption spectroscopy," *Journal of Synchrotron Radiation*, vol. 21, pp. 1140–1147, Sep 2014.
- [13] A. Dvoretzky, P. Erdős, and S. Kakutani, "Nonincrease everywhere of the Brownian motion process," in *Proc. 4th Berkeley Sympos. Math. Statist. and Prob., Vol. II*, pp. 103–116, Univ. California Press, Berkeley, Calif., 1961.
- [14] J. Li, S. Ghoshal, W. Liang, M.-T. Sougrati, F. Jaouen, B. Halevi, S. McKinney, G. McCool, C. Ma, X. Yuan, Z.-F. Ma, S. Mukerjee, and Q. Jia, "Structural and mechanistic basis for the high activity of Fe–N–C catalysts toward oxygen reduction," *Energy Environ. Sci.*, vol. 9, pp. 2418–2432, 2016.
- [15] B. Ravel and M. Newville, "ATHENA, ARTEMIS, HEPHAESTUS: data analysis for X-ray absorption spectroscopy using IFEFFIT," *Journal of synchrotron radiation*, vol. 12, no. 4, pp. 537–541, 2005.
- [16] J. Timoshenko, D. Lu, Y. Lin, and A. I. Frenkel, "Supervised machine-learning-based determination of three-dimensional structure of metallic nanoparticles," *The Journal of Physical Chemistry Letters*, vol. 8, no. 20, pp. 5091–5098, 2017. PMID: 28960990.
- [17] C. Zheng, K. Mathew, C. Chen, Y. Chen, H. Tang, A. Dozier, J. J. Kas, F. D. Vila, J. J. Rehr, L. F. Piper, *et al.*, "Automated generation and ensemble-learned matching of X-ray absorption spectra," *npj Computational Materials*, vol. 4, no. 1, p. 12, 2018.
- [18] I. Miyazato, L. Takahashi, and K. Takahashi, "Automatic oxidation threshold recognition of XAFS data using supervised machine learning," *Molecular Systems Design & Engineering*, 2019.
- [19] S. Mallat, *A wavelet tour of signal processing*. Elsevier/Academic Press, Amsterdam, third ed., 2009. The sparse way, With contributions from Gabriel Peyré.
- [20] T. Hastie, R. Tibshirani, and J. Friedman, *The elements of statistical learning*. Springer Series in Statistics, Springer, New York, second ed., 2009. Data mining, inference, and prediction.
- [21] The idea is based on a construction by Riesz, in what became known as the Rising Sun Lemma [34, Lemma 3.5], developed with the intent of understanding the pointwise behavior of continuous functions. In our case, we are interested in reducing the oscillation of the function in the sense of Def. I.4, which is exactly what the Rising Sun operator does.
- [22] B. Ravel and M. Newville, "ATHENA, ARTEMIS, HEPHAESTUS: data analysis for X-ray absorption spectroscopy using IFEFFIT," *Journal of Synchrotron Radiation*, vol. 12, pp. 537–541, Jul 2005.
- [23] This is similar to the role of dilation and translation parameters in Wavelet theory with regards to resolution. The analogy is limited to the role of parameters, and do not extend beyond that because we are not doing time-frequency analysis [19, 35].
- [24] R. Monteiro, I. Miyazato, and K. Takahashi, "Rising Sun Envelope Method: git-hub." https://github.com/rafael-a-monteiro-math/Rising_Sun_Envelope_Method, 2019.
- [25] P. Larkin, *Infrared and Raman spectroscopy: principles and spectral interpretation*. Elsevier, 2017.
- [26] P. Ewels, T. Sikora, V. Serin, C. P. Ewels, and L. Lajaunie, "A complete overhaul of the electron energy-loss spectroscopy and x-ray absorption spectroscopy database: eelsdb.eu," *Microscopy and Microanalysis*, vol. 22, pp. 717–724, 2 2016.
- [27] B. Lafuente, R. T. Downs, H. Yang, and N. Stone, "The power of databases: the ruff project," in *Highlights in mineralogical crystallography*, pp. 1–29, Walter de Gruyter GmbH, 2016.
- [28] I. Goodfellow, Y. Bengio, and A. Courville, *Deep learning*. MIT press, 2016.
- [29] K. Mathew, C. Zheng, D. Winston, C. Chen, A. Dozier, J. J. Rehr, S. P. Ong, and K. A. Persson, "High-throughput computational X-ray absorption spectroscopy," *Scientific data*, vol. 5, p. 180151, 2018.
- [30] K. T. Butler, D. W. Davies, H. Cartwright, O. Isayev, and A. Walsh, "Machine learning for molecular and materials science," *Nature*, vol. 559, no. 7715, p. 547, 2018.
- [31] K. Takahashi and Y. Tanaka, "Materials informatics: a journey towards material design and synthesis," *Dalton Transactions*, vol. 45, no. 26, pp. 10497–10499, 2016.
- [32] "Hokkaido university catalysis research center xafs database." https://www.cat.hokudai.ac.jp/catdb/index.php?action=xafs_dbinpbrowse&selection=2&r=86. (Accessed on 09/12/2019).
- [33] "Xas spectra library (beta)." <http://cars.uchicago.edu/xaslib/search>. (Accessed on 09/12/2019).
- [34] E. M. Stein and R. Shakarchi, *Real analysis*, vol. 3 of *Princeton Lectures in Analysis*. Princeton University Press, Princeton, NJ, 2005. Measure theory, integration, and Hilbert spaces.
- [35] I. Daubechies, *Ten lectures on wavelets*, vol. 61 of *CBMS-NSF Regional Conference Series in Applied Mathematics*. Society for Industrial and Applied Mathematics (SIAM), Philadelphia, PA, 1992.